Iron-Based Oxygen Scavengers on Mesoporous Silica Nanospheres

Yanling He, Abdul Khaleed, Po Shan Lo, Ishaq Ahmad, Alan Man Ching Ng,* and Aleksandra B. Djurišić*

Read Online

ACCESS | Metrics & More | Article Recommendations | Supporting Information

ABSTRACT: Iron-based materials are among the most commonly used oxygen scavengers. Here, we investigated the mesoporous silica nanosphere (MSN)-supported iron-based scavengers, such as FeO_x nanoparticles and different atomic layer deposition (ALD) coatings (FeO_x and Fe). We found that the scavenger performance is a result of a complex interplay between available Brunauer−Emmett−Teller surface area and the scavenger composition, with the combination of infiltrated nanoparticles and Fe-ALD coating resulting in the best performance. When the glucose-based treatment of MSN is used to further enhance oxygen scavenging capacity, Fe-ALD coating yields the best performance, with a high oxygen adsorption capacity of 126.8 mL/g. ALD deposition of Fe represents a versatile method to introduce Fe-based oxygen scavengers onto different supports, and it can facilitate the integration of scavengers with different types of packaging, as the deposition can be performed at a low temperature of 150 °C.

Fe precursor MSNs

(a) 1st pulse of precursor
(b) Purge
(c) 2nd pulse of precursor
(d) Purge
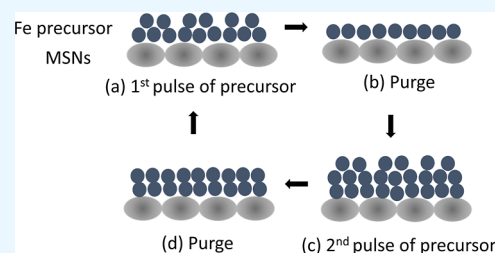
INTRODUCTION

Oxygen scavengers are of significant interest for food packaging applications.[1−12] Oxidative degradation is one of the main mechanisms of food spoilage, and it results in undesirable changes in the food, such as the degradation of nutritional content of the food (due to the degradation of essential fatty acids, vitamins, and proteins), the degradation of odor and taste (due to rancidity), and color change (due to pigment degradation).[1] To reduce spoilage of the food and increase its shelf-life, oxygen scavengers are commonly used in a variety of packaged foods.[1] The scavengers are commonly based on iron, although other types of scavengers are also available, such as those based on other metals (cobalt, palladium, and platinum), organic acids (gallic acid and ascorbic acid), photosensitive dyes, unsaturated organic molecules, enzymes, spores, and yeasts.[1,2] Iron powder packed in sachets remains the most commonly used scavenger.[2,3] These scavengers commonly require the presence of water for scavenging action.[3] The oxygen scavenging capacity of an iron-based scavenger can be improved if nanoparticles instead of micron-sized particles/conventional iron powder are used.[2,4] The nanoparticles also have an advantage of scavenger operation under both wet and dry conditions.[4] Due to the increased surface area, nanosized iron particles enable fast scavenger response and increased adsorption capacity.[4,5] To suppress unwanted aggregation of nanoparticles, their preparation on supports such as montmorillonite clay[6−9] and kaolinite[10] has also been explored, and integration of zero-valent iron nanoparticles with clay is of significant interest for preparation of improved oxygen barrier materials.[6−10] In addition, mesoporous silica nanospheres (MSN) have been explored for oxygen scavenging applications in our previous work.[11]

While zero valent iron nanoparticles exhibit highly promising oxygen scavenging properties due to high reactivity of Fe^0 and iron-containing nanomaterials are generally considered to have low toxicity, concerns over the toxicity of nanoscale zero-valent iron has been rising in recent years.[13−15] As it is known that the toxicity of iron NPs decreases as their surface gets oxidized,[13] and iron oxide nanomaterials are generally considered non-toxic and of interest for medical applications,[16,17] we explored the possibility of using iron oxide nanoparticles as a more stable and less toxic alternative oxygen scavengers. The prepared nanoparticles were investigated alone and infiltrated inside the MSN. We found that infiltration of nanoparticles inside MSN enables an increase in oxygen adsorption capacity, likely due to suppression of nanoparticle aggregation. Similar performance to FeO_x NPs can be obtained by atomic layer deposition (ALD) of FeO_x on MSN, but combination of ALD coating and NP infiltration yields variable results (depending on the type of coating), as the coating increases the amount of iron but decreases the overall surface area available for adsorption. The effect of ALD coating composition on the oxygen scavenging performance is discussed.
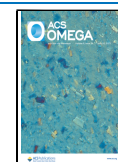
■ RESULTS AND DISCUSSION

Figure S1 shows the transmission electron microscopy (TEM) images of FeO$_x$ nanoparticles (NPs)[18] and FeO$_x$ NPs infiltrated into MSN, while energy-dispersive X-ray (EDX) mapping of FeO$_x$ NPs infiltrated into MSN is shown in Figure 1. In addition, samples with FeO$_x$ and Fe coatings deposited by

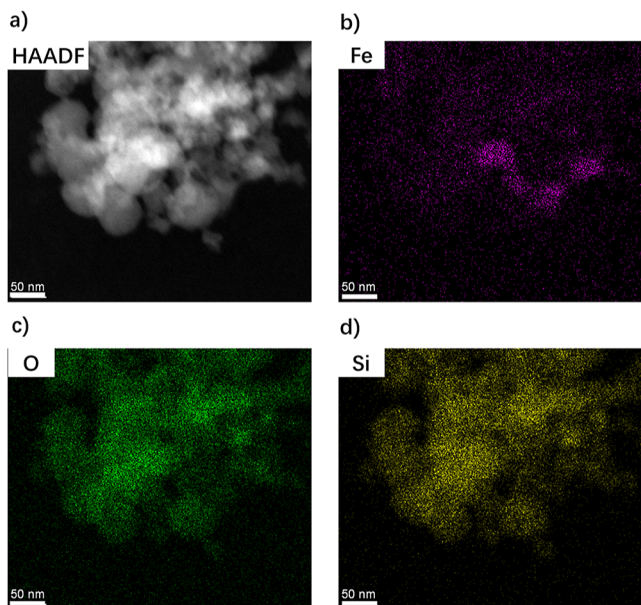are indeed amorphous, while FeO$_x$ NPs show a weak pattern corresponding to the presence of Fe$_2$O$_3$.

To further characterize the composition and structure of the samples, EDX mapping was performed. Obtained results for FeO$_x$ and Fe ALD-coated MSN are shown in Figures 3 and 4,
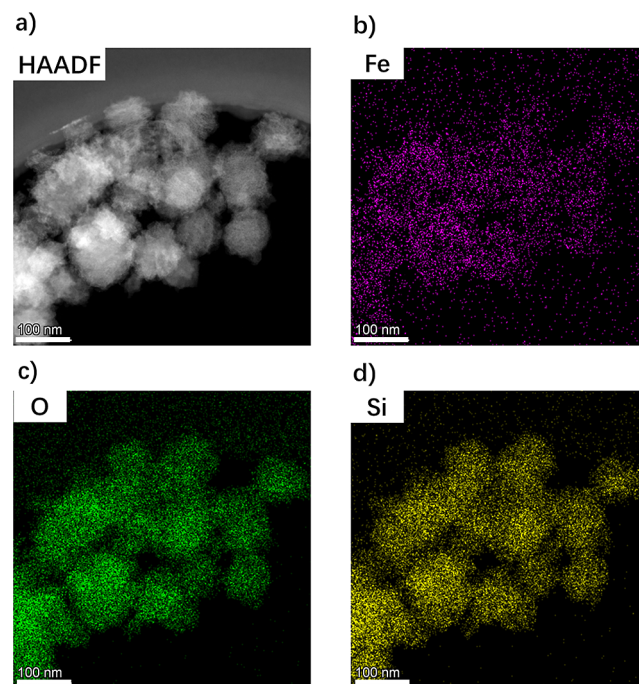

Figure 1. EDX mapping of FeO$_x$ NPs in MSN.

Figure 3. EDX mapping of FeO$_x$ ALD on MSN.

ALD were prepared. TEM images and selected area electron diffraction (SAED) images of MSN with different (Fe and FeO$_x$) ALD coatings, FeO$_x$ NPs and FeO$_x$ NP samples infiltrated into MSN, and ALD FeO$_x$ on FeO$_x$ NPs in MSN are shown in Figure 2. From SAED, we can observe that MSN and both types of ALD coatings are amorphous, while samples with NPs are predominantly amorphous with a small amount of the crystalline phase. To identify this phase, XRD measurements have been performed and obtained results are shown in Figure S5. We can see that all samples except samples with FeO$_x$ NPs

respectively, while the EDX mapping of the sample combining MSN, FeO$_x$ NPs, and ALD deposition of FeO$_x$ coating is shown in Figure S3. HRTEM images of different ALD coatings are shown in Figure 5. We can observe that ALD enables deposition of uniform amorphous coating, in agreement with no evidence of crystallinity obtained from SAED and XRD. From the obtained results, successful incorporation of nanoparticles, as well as coating with the Fe-containing layer by ALD (for both Fe- and FeO$_x$) is evident. Sample composition and stoichiometry has been investigated by
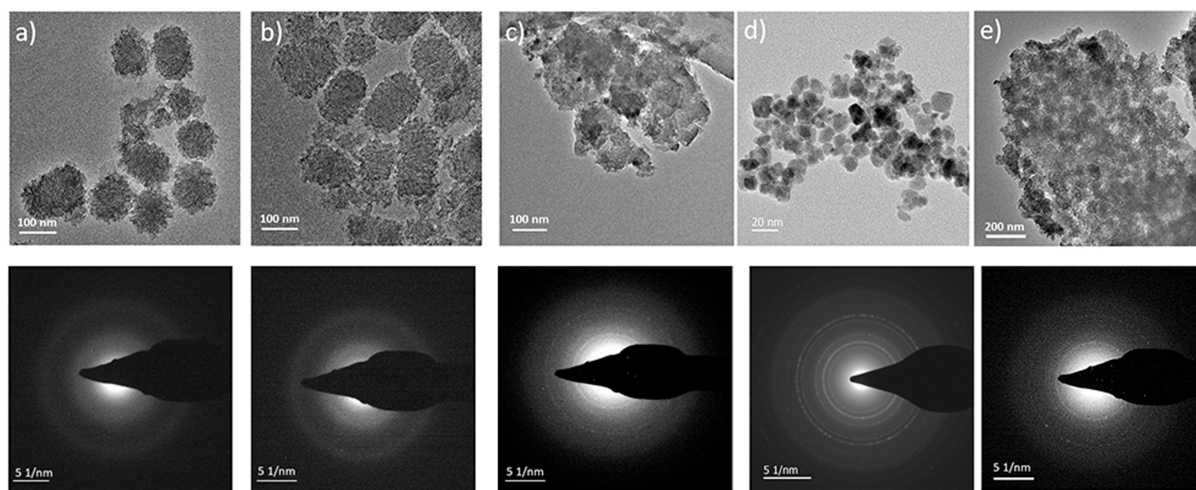

Figure 2. TEM (top) and SAED (bottom) images of (a) ALD FeO$_x$ on MSN, (b) ALD Fe on MSN, (c) FeO$_x$ NPs in MSN, (d) FeO$_x$ NPs, and (e) ALD FeO$_x$ on FeO$_x$ NPs in MSN.

Figure 4. EDX mapping of Fe ALD on MSN.

Table 1. BET Surface Areas and Oxygen Adsorption Capacity of Different Samples

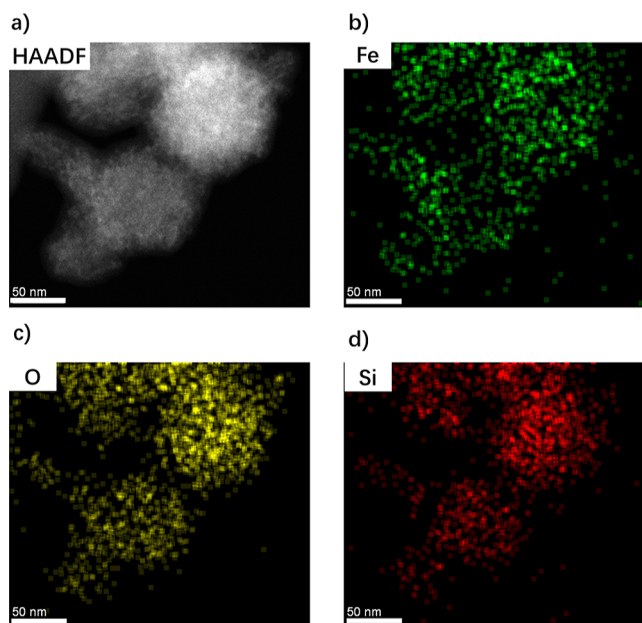| sample	BET surface area (m^2/g)	absorbed oxygen (mL/g)
MSNs	841.6	0.0
FeO_x NPs	134.7	28.0
FeO_x NPs in MSNs	549.7	37.4
FeO_x ALD on MSNs	779.2	28.3
FeO_x ALD on FeO_xNPs in MSNs	504.2	34.4
Fe ALD on MSNs	760.4	55.3
Fe ALD on FeO_x NPs in MSNs	730.1	58.7
MSN-glucose	673.7	119.7
Fe ALD on MSNs-glucose	617.4	126.8
FeO_x ALD on MSNs-glucose	615.9	105.5
FeO_x ALD on FeO_x NPs in MSNs-glucose	430.6	101.9
FeO_x NPs in MSNs-glucose	504.6	108.6
Fe ALD on FeO_x NPs in MSNs-glucose	447.9	114.9

EDX and X-ray photoelectron spectroscopy (XPS), and obtained results are summarized in Table S1. We can conclude that FeO_x NPs consist of predominant amorphous FeO phase with small Fe_2O_3 content. FeO_x ALD coating likely contains a higher share of Fe_2O_3 compared to FeO from a lower Fe/O ratio, while Fe ALD coating yields high Fe/O ratio, likely due to the presence of metallic Fe.

To further evaluate the potential of different samples for oxygen scavenging applications Brunauer−Emmett−Teller (BET) surface areas and oxygen scavenging performance were determined, as summarized in Table 1 (corresponding isotherms are shown in Figures S4−S6). For comparison, reported performances of various iron-based scavengers in the literature are summarized in Table S2. We can observe that FeO_x NPs exhibit oxygen adsorption capacity comparable to that of commercial scavengers (23.5−37.2 mL/g, measured under 53−57% RH). The oxygen adsorption capacity increases after infiltration into MSN, which are inert with respect to oxygen. The FeO_x coating of MSN by ALD[11,19−23] yields similar oxygen scavenging performance to FeO_x NPs. We can observe that the surface area of ALD coated samples is significantly higher than that of FeO_x NPs in MSN, but the oxygen scavenging performance is worse despite higher surface area. This is likely due to the fact that oxygen adsorption capacity is dependent both on the surface area and sample

composition, i.e., availability of surface Fe which can be further oxidized. Both FeO_x ALD coating and FeO_x NPs contain FeO and Fe_2O_3, but in different proportions as evident from differences in sample stoichiometry (Table S1). The higher Fe_2O_3 content of FeO_x-ALD coating would result in decreased oxygen scavenging capacity despite the increased surface area. The combination of NPs and ALD coating results in reduced oxygen scavenging capacity compared to FeO_x NPs in MSNs and increased oxygen scavenging capacity compared to FeO_x ALD on MSNs, likely a result of reduced surface area compared to FeO_x NPs in MSNs (and possibly increased Fe^{3+} content due to ALD coating) and increased Fe^{2+} content compared to FeO_x ALD on MSNs due to the presence of FeO_x NPs.

The samples with Fe-ALD coating exhibit significant improvements in oxygen scavenging capacity, as expected since the oxygen adsorption capacity for oxidation of Fe^0 into Fe^{2+}/Fe^{3+} is higher than that for oxidation of Fe^{2+} to Fe^{3+}. In this case, the combination of FeO_x NPs and ALD coating results in further enhancement of the performance.

To understand the mechanism of oxygen scavenging of different samples, XPS measurements before and after exposure to atmosphere for oxygen adsorption were conducted. Obtained results are shown in Figure 6 and summarized in Table 2, where the ratios of Fe^0, Fe^{2+}, and Fe^{3+} in different samples were determined from fitting the Fe 3p spectra.[24−27] We can observe that for both FeO_x NPs and FeO_x coating by ALD, oxygen scavenging occurs due to oxidation of Fe^{2+} to Fe^{3+}. The higher starting Fe^{2+}/Fe^{3+} ratio of
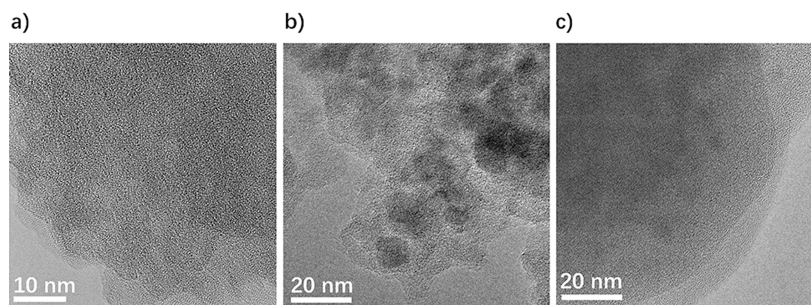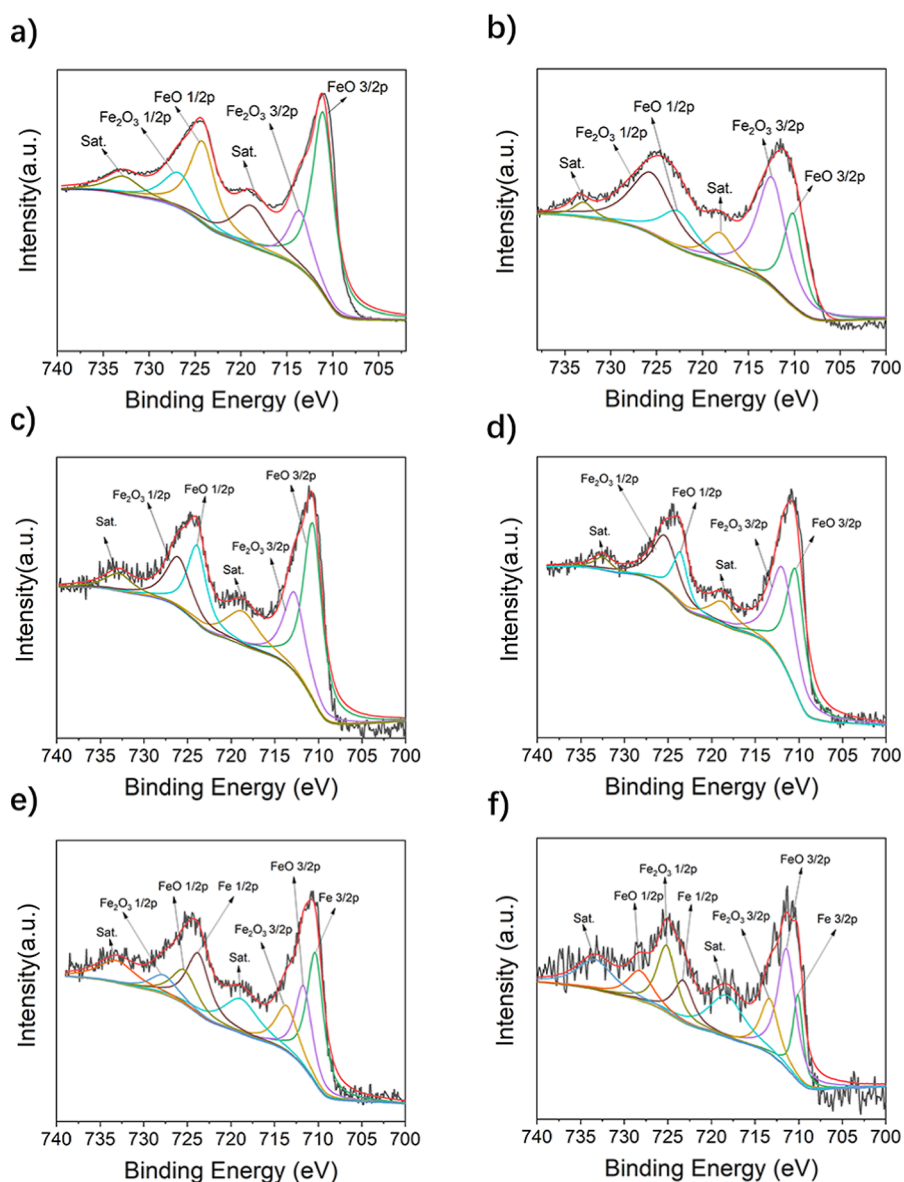

Figure 5. HRTEM images of (a) Fe ALD on MSN; (b) FeO_x ALD on MSN with FeO_x NPs; and (c) FeO_x ALD on MSN.

Figure 6. XPS Fe spectra of (a,b) FeO$_x$ NPs fresh and 24 h; (c,d) FeO$_x$ ALD on MSN fresh and 24 h; and (e,f) Fe ALD on MSN fresh and 24 h.

Table 2. XPS Fitting Results for Fe^0, Fe^{2+}, and Fe^{3+} Content in Different Samples

samples	Fe^{2+}/Fe^{3+}	Fe/Fe^{3+}	Fe/Fe^{2+}
FeO$_x$ NPs-fresh	3.20	0	0
FeO$_x$ NPs 24 h	0.75	0	0
FeO$_x$ ALD on MSNs-fresh	2.22	0	0
FeO$_x$ ALD on MSNs-24 h	0.78	0	0
Fe ALD on MSNs-fresh	1.77	2.86	1.61
Fe ALD on MSNs-24 h	2.2	1.59	0.72

NPs is likely responsible for higher oxygen adsorption capacity of these samples. The oxygen adsorption capacity is a result of interplay between surface area and iron content in an oxidation state where further oxidation is possible (Fe^0 or Fe^{2+}). Consequently, samples with lower surface area and higher Fe^{2+} content (FeO$_x$ NPs) and samples with higher surface area and lower Fe^{2+} content (FeO$_x$ ALD on MSNs) can exhibit a similar oxygen scavenging performance. For Fe-coated MSN, we can observe a significantly different mode of action. In this case, Fe^0 gets oxidized to Fe^{2+}, and then, Fe^{2+} gets oxidized to Fe^{3+}. Consequently, after 24 h, the Fe^{2+}/Fe^{3+} ratio is increased, while Fe/Fe^{2+} and Fe/Fe^{3+} ratios are both decreased. From the fact that the samples still contain unreacted Fe^0 after 24 h exposure to ambient atmosphere, we can conclude that the reactivity of Fe ALD-coated MSN is not very high and that these samples likely represent a good compromise between reactivity and oxygen adsorption capacity.

To investigate the possibility of further enhancement of oxygen adsorption capacity, we considered glucose-treated MSN samples, as these samples can exhibit high oxygen scavenging capacity.[11] Successful coating with a carbon-containing layer is evident from the TEM images (Figure S7) and EDX mapping of the samples (Figure S8). The glucose treatment enables significant oxygen scavenging capacity, which was attributed to loosely bound oxygen on the surface. To investigate the mechanism of oxygen adsorption, FTIR measurements were conducted, and the obtained results are shown in Figure S9. We can observe a significant enhancement in the intensity, as well as a change in

the position and shape of a broad feature in the spectral range 3200−3700 cm^{-1}, which corresponds to O−H stretching vibrations,[29] as well as the vibration at ∼1640 cm^{-1} corresponding to molecular water.[29] No changes in prominent feature in the range 1000−1120 cm^{-1} corresponding to Si−O−Si vibrations[29] is observed. The shift in the O−H vibrations peak position and the change in the peak shape likely originate from a change in proportions of free O−H and hydrogen-bonded (intra- and inter-molecular) O−H vibrations.[29] The observed changes are consistent with the increase in loosely bound surface oxygen. In the case of glucose-modified MSN, the use of FeO$_x$ NP infiltration results in significant reduction of the available surface area in all cases, and consequently, no enhancement of the oxygen adsorption capacity is obtained. For ALD coating only, there is a smaller loss of BET surface area. However, FeO$_x$ ALD coating results in lower oxygen adsorption capacity compared to glucose-treatment only, while Fe ALD coating is the only condition resulting in the enhancement of oxygen adsorption capacity. Considering the versatility of ALD deposition, the preparation method should be compatible not only with different MSN-based samples investigated in this work but also generally applicable, for example, as a part of multilayer oxygen barriers in packaging. Unlike nanoparticle samples incorporated into extruded polymers, ALD deposited coatings are expected to have excellent mechanical integrity and are unlikely to result in leakage of nanomaterial into the environment.

CONCLUSIONS

We have investigated the oxygen scavenging performance of FeO$_x$ NPs and iron-based coatings deposited by ALD. We found that ALD FeO$_x$ coating results in lower Fe^{2+}/Fe^{3+} ratios compared to FeO$_x$ NPs, while Fe ALD coating results in increased oxygen adsorption capacity due to oxidation of Fe^0 into Fe^{2+}/Fe^{3+}. For combining the FeO$_x$ NPs and ALD-coated MSN for increasing overall oxygen adsorption capacity, there is a complex interplay between the coating composition and reduced surface area after deposition. Thus, for FeO$_x$ NPs infiltrated inside MSN, an increase in oxygen adsorption capacity can be obtained with Fe-ALD coating, but not with FeO$_x$-ALD coating. In addition, Fe-ALD coating is generally applicable to different samples and can be used to enhance oxygen adsorption capacity of glucose-treated MSN, with the highest oxygen adsorption capacity of 126.8 mL/g obtained. Fe-ALD coating is a versatile method for enhancing the oxygen adsorption capacity and also has a potential promise for integration with the packaging as a part of oxygen barriers.

EXPERIMENTAL SECTION

Materials. Tetraethyl orthosilicate (TEOS, purity 99.9%) and cetyl trimethylammonium bromide (CTAB, purity 98%) were obtained from Alfa Aesar. Ethanol (purity 99.8%), NH$_3$·H$_2$O (ACS, 28−30%), and 1,3,5-trimethylbenzene (TMB, purity 98%) were obtained from Energy Chemical. ALD precursor ferrocene (purity 99.999%) was obtained from Sigma-Aldrich. All materials were used as received without further purification.

Synthesis of FeO$_x$ NPs. The NPs were synthesized following a previously reported procedure[18] with minor modifications. Briefly, 12 mL of 0.2 M FeCl$_3$ aqueous solution was poured into 12 mL of 0.5 M NH$_4$OH solution at room temperature and allowed to sonicate for 2 min. 6 mL of

aqueous 0.2 M FeCl$_2$ was then added under sonication and the mixture was poured into 36 mL of 0.5 M NH$_4$OH aqueous solution. The solution was then swirled and stirred for 1 min. The solution was then kept still for 15 min, then magnetically separated, and washed with 200 mL of DI water each time at least five times. Afterward, 1.5 mL of 0.1 M sodium citrate was added under sonication, followed by dropwise addition of 1 mL of 5% sodium hypochlorite solution. The washing process was then repeated to collect the product. The final product was then washed once more under centrifugation at 9000 rpm for 5 min, the supernatant was disposed of, and the colloid was left in vacuum at 50 °C to dry overnight. The resulting big clumps were broken into a coarse powder using a metal spatula to obtain the final product.

Synthesis of MSN and Glucose-Treated MSN. The synthesis of MSNs was reported in our previous work.[11] Briefly, 16 mL of deionized water, 6 mL of ethanol, 0.5 mL of NH$_3$·H$_2$O, and 0.6 g CTAB were mixed and sonicated for 15 min. After the sonication, 0.225 mL of ammonia was added to adjust pH to ∼10 to 11 and the solution was homogenized for 30 min. TMB (0.9 mL) and TEOS (2 mL) were then added with rapid stirring at 800 rpm. After 2 h reaction, the white precipitates were centrifuged at 10,000 rpm for 10 min and purified by ethanol three times. Then, the as-prepared precipitates were dried for 16 h in air at 60 °C. Finally, MSNs obtained by calcination at 550 °C for 10 h in a muffle furnace with a heating rate of 1 °C/min. For the glucose treatment of MSN,[11] 100 mg of MSNs and 60 mg glucose were dispersed into 30 mL of deionized water and stirred for 30 min, followed by ultra-sonication for 10 min and then stirring for another 10 min. The solution was then transferred into a 50 mL Teflon lined stainless steel autoclave and kept at 180 °C for 4 h. The reacted solution was centrifuged and washed by ethanol several times. Prepared samples were then ground and dried at 40 °C under high vacuum.

Synthesis of FeO$_x$ NP Infiltrated MSN. Based on a previously reported procedure,[28] 0.6 g of CTAB is added to a mixture of deionized water, FeO$_x$ NP solution and ethanol (8 mL/8 mL/4 mL). To adjust the pH (pH ∼ 11−12) of the mixture, 0.3 mL of ammonia solution is added. The solution is then sonicated for 15 min to give a homogeneous mixture. TMB (0.9 mL) and TEOS (2 mL) were added to the mixture and stirred for 2 h at 800 rpm. The gel obtained is then centrifuged at 4000 rpm for 30 min and washed with ethanol twice at 4000 rpm for 10 min. The obtained gel is then dried in vacuum at 70 °C overnight. The dried product is ground to give a fine powder and calcined at 550 °C for 5 h at a ramping rate of 1 °C/min to yield FeO$_x$ NPs incorporated in MSN.

ALD Coating of MSN. ALD deposition of Fe and FeO$_x$ coatings were performed on the pre-synthesized MSN powder using a Savannah S200 ALD chamber from Ultratech. The Fe deposition was carried out at a low temperature of 150 °C and ferrocene was used as a precursor heated at 423 K. The pulse time for the ferrocene precursor was 0.5 s, and 10 sccm N$_2$ was purged in between two consecutive ferrocene pulses for 20 s. 100 cycles of Fe were coated on the MSNs. For the deposition of FeO$_x$ coating, ferrocene and water (H$_2$O) were used as precursors.[11] The deposition was carried out at 573 K and the ferrocene precursor was heated up to 423 K to maintain the adequate vapor pressure in the bubbler. One cycle consisted of a 0.01 s pulse of ferrocene with 5 s purge nitrogen and a 0.015 s pulse of water, with 15 s purge nitrogen.

Characterizations. The sample morphologies and EDX mapping were recorded using TEM equipped with EDX analyzer (FEI, Talos) operated at 300 kV. SAED patterns were also acquired at 300 kV. EDX analyses were performed using NOVA Nano SEM450 from FEI. A voltage of 5 kV and high beam current was used for composition analysis. The EDX measurements for overall Fe content determination were carried out on the NP powders and ALD coating samples on MSN powders. Same ALD coatings were deposited on Al substrates (purity 99.999%) for Fe/O ratio detection (since MSN samples contain oxygen).

X-ray photoelectron spectra (XPS) were recorded using an ESCALAB 250Xi from Thermo Fisher equipped with Al Kα (1486.69 eV) X-ray source. The C 1s binding energy of 284.8 eV was used as energy reference. In order to obtain a sufficiently strong signal, one spectrum was obtained under vacuum with an accumulation time of 100 s and five scans. The BET measurements were performed using a Micromeritics ASAP2020 physisorption analyzer with pure nitrogen at 77 K. The FTIR measurements were conducted by a Bruker VERTEX 80v spectrometer. Samples were well mixed and ground with dried potassium bromide (KBr, Sigma-Aldrich). The final concentrations of samples/KBr were ~1% (w/w). The crystal structures of the samples were examined using X-ray diffraction (Rigaku, SmartLab; operated at 40 kV and 150 mA, Cu Kα source).

Oxygen adsorption capacity was determined as described previously.[11] Briefly, measurements carried out using an MapXpert from JC Instruments with a measurement range of 0−100% and a resolution of 0.001%. The sample with the weight of 250 mg was placed in a 350 mL bottle and sealed. The humidity was controlled at 57% in the bottle. 3 mL of the gases were purged within 5 s for testing with an interval of 24 h.

ASSOCIATED CONTENT

Supporting Information

The Supporting Information is available free of charge at https://pubs.acs.org/doi/10.1021/acsomega.3c01242.

Nitrogen adsorption isotherms for the determination of BET surface area and EDX mapping images (PDF)

AUTHOR INFORMATION

Corresponding Authors

Alan Man Ching Ng − *Core Research Facilities, Southern University of Science and Technology, Shenzhen, Guangdong 518055, P. R. China;* orcid.org/0000-0001-7081-8244; Email: ngamc@sustech.edu.cn

Aleksandra B. Djurišić − *Department of Physics, The University of Hong Kong, Hong Kong, Hong Kong SAR, China;* orcid.org/0000-0002-5183-1467; Email: dalek@hku.hk

Authors

Yanling He − *Department of Physics, The University of Hong Kong, Hong Kong, Hong Kong SAR, China*

Abdul Khaleed − *Department of Physics, The University of Hong Kong, Hong Kong, Hong Kong SAR, China*

Po Shan Lo − *Department of Physics, The University of Hong Kong, Hong Kong, Hong Kong SAR, China*

Ishaq Ahmad − *Department of Physics, The University of Hong Kong, Hong Kong, Hong Kong SAR, China*

Complete contact information is available at:
https://pubs.acs.org/10.1021/acsomega.3c01242

Author Contributions

A. M. C. N. and A. B. D. designed the whole study, analyzed and interpreted results, and wrote the manuscript. Y. H. conducted ALD deposition and various sample characterizations. A. K. synthesized iron oxide nanoparticles, and P. S. L. and I. A. prepared MSN samples. All co-authors provided input to the final version of the manuscript.

Notes

The authors declare no competing financial interest.

REFERENCES

(1) Vilela, C.; Kurek, M.; Hayouka, Z.; Röcker, B.; Yildirim, S.; Antunes, M. D. C.; Nilsen-Nygaard, J.; Pettersen, M. K.; Freire, C. S. R. A Concise Guide to Active Agents for Active Food Packaging. *Trends Food Sci. Technol.* **2018**, *80*, 212−222.

(2) Dey, A.; Neogi, S. Oxygen Scavengers for Food Packaging Applications: A Review. *Trends Food Sci. Technol.* **2019**, *90*, 26−34.

(3) Miltz, J.; Perry, M. Evaluation of the Performance of Iron-Based Oxygen Scavengers, with Comments on Their Optimal Applications. *Packag. Technol. Sci.* **2005**, *18*, 21−27.

(4) Foltynowicz, Z.; Bardenshtein, A.; Sängerlaub, S.; Antvorskov, H.; Kozak, W. Nanoscale, Zero Valent Iron Particles for Application as Oxygen Scavenger in Food Packaging. *Food Packag. Shelf Life* **2017**, *11*, 74−83.

(5) Mu, H.; Gao, H.; Chen, H.; Tao, F.; Fang, X.; Ge, L. A Nanosised Oxygen Scavenger: Preparation and Antioxidant Application to Roasted Sunflower Seeds and Walnuts. *Food Chem.* **2013**, *136*, 245−250.

(6) Kombaya-Touckia-Linin, E.-M.; Gaucel, S.; Sougrati, M. T.; Khederlou, K.; Pen, N.; Stievano, L.; Gontard, N.; Guillard, V. Hybrid Iron Montmorillonite Nano-Particles as an Oxygen Scavenger. *Chem. Eng. J.* **2019**, *357*, 750−760.

(7) Khalaj, M.-J.; Ahmadi, H.; Lesankhosh, R.; Khalaj, G. Study of Physical and Mechanical Properties of Polypropylene Nanocomposites for Food Packaging Application: Nano-Clay Modified with Iron Nanoparticles. *Trends Food Sci. Technol.* **2016**, *51*, 41−48.

(8) Kombaya-Touckia-Linin, E.-M.; Gaucel, S.; Sougrati, M. T.; Stievano, L.; Gontard, N.; Guillard, V. Elaboration and Characterization of Active Films Containing Iron-Montmorillonite Nanocomposites for O$_2$ Scavenging. *Nanomaterials* **2019**, *9*, 1193.

(9) Khederlou, K.; Bagheri, R.; Shojaei, A.; Gontard, N.; Tamsilian, Y. Oxygen Scavenging Hybrid Nanostructure: Localization of Different Iron Nanoparticles on Montmorillonite Clays Host. *ACS Omega* **2022**, *7*, 16391−16401.

(10) Busolo, M. A.; Lagaron, J. M. Oxygen Scavenging Polyolefin Nanocomposite Films Containing an Iron Modified Kaolinite of Interest in Active Food Packaging Applications. *Innovative Food Sci. Emerging Technol.* **2012**, *16*, 211−217.

(11) He, Y.; Hu, X.; Xu, M.; Ng, A. M. C.; Djurišić, A. B. Mesoporous Silica Nanosphere-Based Oxygen Scavengers. *Microporous Mesoporous Mater.* **2021**, *327*, 111426.

(12) Janjarasskul, T.; Suppakul, P. Active and Intelligent Packaging: The Indication of Quality and Safety. *Crit. Rev. Food Sci. Nutr.* **2018**, *58*, 808−831.

(13) Lei, C.; Sun, Y. Q.; Tsang, D. C. W.; Lin, D. H. Environmental transformations and ecological effects of iron-based nanoparticles. *Environ. Pollut.* **2018**, *232*, 10−30.

(14) Kirthi, A. V.; Kumar, G.; Pant, G.; Pant, M.; Hossain, K.; Ahmad, A.; Alshammari, M. B. Toxicity of Nanoscaled Zero-Valent Iron Particles on Tilapia, Oreochromis mossambicus. *ACS Omega* **2022**, *7*, 47869−47879.

(15) Rabeh, I.; Telahigue, K.; Hajji, T.; Mdaini, Z.; Nechi, S.; Chelbi, E.; El Cafsi, M.; Mhadhbi, L. Impacts of engineered iron nanoparticles on oxidative stress, fatty acid composition, and histo-architecture of the smooth scallop Flexopecten glaber. *Environ. Sci. Pollut. Res.* **2022**, *29*, 78396−78413.

(16) Ling, D. S.; Hyeon, T. H. Chemical Design of Biocompatible Iron Oxide Nanoparticles for Medical Applications. *Small* **2013**, *9*, 1450−1466.

(17) Malhotra, N.; Lee, J. S.; Liman, R. A. D.; Ruallo, J. M. S.; Villaflores, O. B.; Ger, T. R.; Hsiao, C. D. Potential Toxicity of Iron Oxide Magnetic Nanoparticles: A Review. *Molecules* **2020**, *25*, 3159.

(18) Babic, M.; Horák, D.; Trchová, M.; Jendelová, P.; Glogarová, K.; Lesný, P.; Herynek, V.; Hájek, M.; Syková, E. Poly(L-Lysine)-Modified Iron Oxide Nanoparticles for Stem Cell Labeling. *Bioconjugate Chem.* **2008**, *19*, 740−750.

(19) Paul, R.; Reifenberger, R. G.; Fisher, T. S.; Zemlyanov, D. Y. Atomic Layer Deposition of FeO on Pt(111) by Ferrocene Adsorption and Oxidation. *Chem. Mater.* **2015**, *27*, 5915−5924.

(20) Aronniemi, M.; Saino, J.; Lahtinen, J. Characterization and Gas-Sensing Behavior of an Iron Oxide Thin Film Prepared by Atomic Layer Deposition. *Thin Solid Films* **2008**, *516*, 6110−6115.

(21) Onn, T. M.; Monai, M.; Dai, S.; Arroyo-Ramirez, L.; Zhang, S.; Pan, X.; Graham, G. W.; Fornasiero, P.; Gorte, R. J. High-Surface-Area, Iron-Oxide Films Prepared by Atomic Layer Deposition on γ-Al_2O_3. *Appl. Catal., A* **2017**, *534*, 70−77.

(22) Tanskanen, A.; Karppinen, M. Iron-Based Inorganic-Organic Hybrid and Superlattice Thin Films by ALD/MLD. *Dalton Trans.* **2015**, *44*, 19194−19199.

(23) Selvaraj, S.; Moon, H.; Yun, J.-Y.; Kim, D.-H. Iron Oxide Grown by Low-Temperature Atomic Layer Deposition. *Korean J. Chem. Eng.* **2016**, *33*, 3516−3522.

(24) Yamashita, T.; Hayes, P. Analysis of XPS Spectra of Fe^{2+} and Fe^{3+} Ions in Oxide Materials. *Appl. Surf. Sci.* **2008**, *254*, 2441−2449.

(25) Grosvenor, A. P.; Kobe, B. A.; Biesinger, M. C.; McIntyre, N. S. Investigation of Multiplet Splitting of Fe 2p XPS Spectra and Bonding in Iron Compounds. *Surf. Interface Anal.* **2004**, *36*, 1564−1574.

(26) Lesiak, B.; Jablonski, A.; Zemek, J.; Jiricek, P.; Čerňanský, M. Studies of Iron and Iron Oxide Layers by Electron Spectroscopes. *Appl. Surf. Sci.* **2005**, *252*, 330−338.

(27) Yan, L. P.; Gopinath, S. C. B.; Anbu, P.; Kasim, F. H.; Zulhaimi, H. I.; Yaakub, A. R. W. Characterization and Anti-Bacterial Potential of Iron Oxide Nanoparticle Processed Eco-Friendly by Plant Extract. *Prep. Biochem. Biotechnol.* **2020**, *50*, 1053−1062.

(28) Ahmad, I.; Shan, L. P.; Djurišić, A. B.; He, Y. L.; Ng, A. M. C. Metal oxide nanoparticles incorporated mesoporous silica nano-spheres for oxygen scavenging. *SPIE Photonics West*, 2022; Vol. *12002*, p 120020O.

(29) Socrates, G. *Infrared and Raman Characteristic Group Frequencies*; John Wiley & Sons: Chichester, England, 2001.